Single-phase hybrid micro-channel/micro-jet impingement cooling

Myung Ki Sung, Issam Mudawar *

*Boiling and Two-Phase Flow Laboratory (BTPFL), Purdue University International Electronic Cooling Alliance (PUIECA),
Mechanical Engineering Building, 585 Purdue Mall, West Lafayette, IN 47907-2088, USA*

Abstract

A new hybrid cooling scheme is proposed for high-flux thermal management of electronic and power devices. This scheme combines the cooling benefits of micro-channel flow and micro-jet impingement with those of indirect refrigeration cooling. Experiments were performed to assess single-phase cooling performance using HFE 7100 as working fluid. Excellent predictions were achieved using the standard k–ε model. The proposed cooling scheme is shown to involve complex interactions of impinging jets with micro-channel flow. Increasing jet velocity allows jets to penetrate the micro-channel flow toward the heated surface, especially in shallow micro-channels, greatly decreasing wall temperature. Despite the relatively poor thermophysical properties of HFE 7100, the proposed cooling scheme facilitated the dissipation of 304.9 W/cm^2 without phase change; further improvement is possible by increasing jet velocity and/or decreasing coolant temperature. In addition to the numerical predictions, a superpositioning technique is introduced that partitions the heat transfer surface into zones that are each dominated by a different heat transfer mechanism, and assigning a different heat transfer coefficient value to each zone. Using this technique, a new correlation is developed that fits the data with a mean absolute error of 6.04%.
© 2008 Elsevier Ltd. All rights reserved.

1. Introduction

Spurred by micro-miniaturization of electronic components and greatly increased component and circuit density in electronic and power devices, heat dissipation has become a primary concern in the design of such devices. High performance cooling schemes are therefore becoming increasingly important to the development of high-end devices.

Removal of the heat dissipated by an electronic or power device is only one aspect of a cooling solution. Another is the need to maintain device temperature safely below a limit that is dictated by both material and performance concerns. This is especially the case with devices that dissipate very large heat fluxes. For a finite thermal resistance across the cooling fluid and various materials comprising an electronic package, dissipating high heat fluxes while maintaining an acceptably low device temperature

requires decreasing the temperature of the working fluid. Low temperature electronic cooling using indirect refrigeration cooling of the working fluid is an effective means for achieving this objective. Low temperature cooling also improves the performance of an electronic device by decreasing current leakage. Naeemi and Meindl [1] showed the performance of a CMOS chip at −100 °C could be as high as 4.3 times the performance at 85 °C. Schmidt and Notohardjono [2] also showed low temperature cooling offers orders of magnitude improvement in reliability.

To combat cooling challenges, a myriad of liquid cooling schemes have been developed and tested, mostly since the early 1980s. Of those, jet impingement and micro-channel heat sinks have emerged as the two most powerful thermal solutions for such next generation devices as microprocessors, laser diodes, radars and X-ray anodes [3].

Jet impingement cooling has been investigated both experimentally [4–7] and numerically [8–10]. These studies demonstrated the effectiveness of jet impingement at maintaining very low thermal resistances, especially in the jet's stagnation zone. A key drawback in using a single jet to

---

* Corresponding author. Tel.: +1 765 494 5705; fax: +1 765 494 0539.
E-mail address: mudawar@ecn.purdue.edu (I. Mudawar).

Nomenclature

a	empirical constant		T_{in}	fluid inlet temperature
A_t	top test surface area of copper heating block		T_{tci}	temperature measured by thermocouple tc$i$ ($i = 1$–4)
b	empirical constant		u	velocity component in x direction
c	empirical constant		U_i	Cartesian components of velocity
C_1, C_2, C_3	empirical constants		U_{jet}	mean jet velocity
C_1, C_2, C_μ	turbulence model constants		v	velocity component in y direction
c_p	specific heat at constant pressure		w	velocity component in z direction
D_{jet}	diameter of micro-jet		W	width of unit cell
G	production of turbulent energy		W_{ch}	width of micro-channel
H	height of unit cell		W_w	half-width of copper wall separating micro-channels
H_{ch}	height of micro-channel		x	Cartesian coordinate
H_{jet}	height (length) of micro-jet		y	Cartesian coordinate
H_{th}	height from thermocouple hole to unit cell bottom boundary		z	Cartesian coordinate
H_w	height from unit cell bottom boundary to test surface			
h	convective heat transfer coefficient, $q''_{eff}/(T_w - T_{in})$		*Greek symbols*	
			ε	dissipation rate of turbulent kinetic energy
k	thermal conductivity; turbulent kinetic energy		μ	dynamic viscosity
L	length of unit cell (also length of micro-channel)		μ_t	eddy viscosity
L_{jet}	jet pitch		v	kinematic viscosity
L_1, L_2, L_3, L_4	distance between thermocouple holes		ρ	density
$\dot{m}$	mass flow rate		σ_ε	empirical constant in k and ε transport equations
n	outer normal coordinate at interface between solid and liquid		σ_k	empirical constant in k and ε transport equations
N_{jet}	number of micro-jets per single micro-channel			
Nu	Nusselt number		*Subscripts*	
p	perimeter of micro-channel		ch	channel
P	pressure		f	fluid
Pr	Prandtl number		in	inlet
Pr_t	turbulent Prandtl number		s	solid
P_W	electrical power supplied to copper heating block		t	turbulent
			tc$i$	thermocouple ($i = 1$–4)
q''_{eff}	effective heat flux based on top test surface area of copper heating block, P_W/A_t		w	wall
			Γ	interface between solid and liquid
Re	Reynolds number			
T	temperature			

cool the surface of an electronic device is large variation of surface temperature caused by a sharp reduction in the heat transfer coefficient away from the stagnation zone. Multiple jets are often used to attenuate those variations by creating multiple, closely spaced stagnation zones. Here too, problems arise due to flow blockage between closely spaced jets especially for jets that are situated towards the center of the device surface. Blockage for the central jets can also greatly complicate coolant distribution and exit of the spent fluid [5]. Clearly, better means are needed to capitalize upon the merits of multiple jet impingement while facilitating a more advantageous flow distribution inside of, and exit from, a cooling module.

Micro-channel heat sinks have been studied quite extensively for chip cooling applications. In an early often-cited

study, Tuckerman and Pease demonstrated heat removal rates up to 790 W/cm² using water as working fluid [11]. A key advantage of micro-channel heat sinks is their ability to achieve high heat transfer coefficients using coolant flow rates that are far smaller than those required with jet impingement. However, this advantage is realized with a very large temperature rise along the direction of fluid flow as well as large pressure drop, both of which are very undesirable in electronics cooling. In addition to experimental work, several numerical studies have been published on the fluid flow and heat transfer characteristics of micro-channel heat sinks [12–14]. Qu and Mudawar [14] demonstrated that the conventional Navier–Stokes and energy equations provide accurate prediction of a heat sink's single-phase heat transfer characteristics.

Clearly, both jet impingement and micro-channel heat sinks can dissipate the high heat fluxes anticipated in future high performance devices. However, as explained above, both have drawbacks. Recently, the authors of the present study proposed an effective means for capitalizing upon the merits of cooling schemes while alleviating some their shortcomings [15]. They showed how a 'hybrid' cooling scheme consisting of slot jets that feed fluid into micro-channels can meet the challenges of high performance electronic devices by facilitating the dissipation of high heat fluxes while also maintaining uniformity in the device surface temperature.

In this study, a new hybrid cooling scheme is discussed that ensures excellent heat removal capability while maintaining fairly uniform surface temperature. This scheme involves feeding coolant from a series of circular micro-jets to each micro-channel in a modified micro-channel heat sink module. Numerical simulation is first used to select key geometrical parameters, and the selected geometry is then examined experimentally. A superpositioning technique is used to develop a single-phase heat transfer correlation for this new cooling scheme.

2. Experimental methods

2.1. Flow loop

Fig. 1 shows the flow loop that was configured to supply 3M Novec liquid HFE 7100 to a test module that housed

the hybrid cooling configuration. This dielectric liquid was supplied from a reservoir with the aid of a centrifugal pump. The liquid first passed through a heat exchanger, where its temperature was greatly reduced by sensible heat exchange to refrigerant in a two-stage cascade chiller. The mass flow rate of HFE 7100 was measured by a Coriolis flow meter before the liquid entered the test module. The coolant flow was throttled using two control valves, one located upstream and the second downstream of the test module. The downstream valve also set the desired test module outlet pressure. After exiting the test module, the liquid returned to the reservoir to complete a full flow cycle.

2.2. Test module

Fig. 2 illustrates the layered construction and assembly of the test module. The micro-channels were machined into the top surface of a copper heating block. The test module also included a micro-jet plate, an upper plenum plate, a lower support plate, and 16 cartridge heaters. Fig. 3 shows further details and key dimensions of the heating block. This block was tapered in two steps to improve temperature uniformity along its top $1.0 \times 2.0 \, \text{cm}^2$ test surface. Machined into its top surface were five 1 mm wide and 3 mm deep slots. Six copper-constantan (type-T) thermocouples were inserted below the test surface to monitor its temperature. Sixteen holes were drilled into the large underside of the heating block to accommodate the
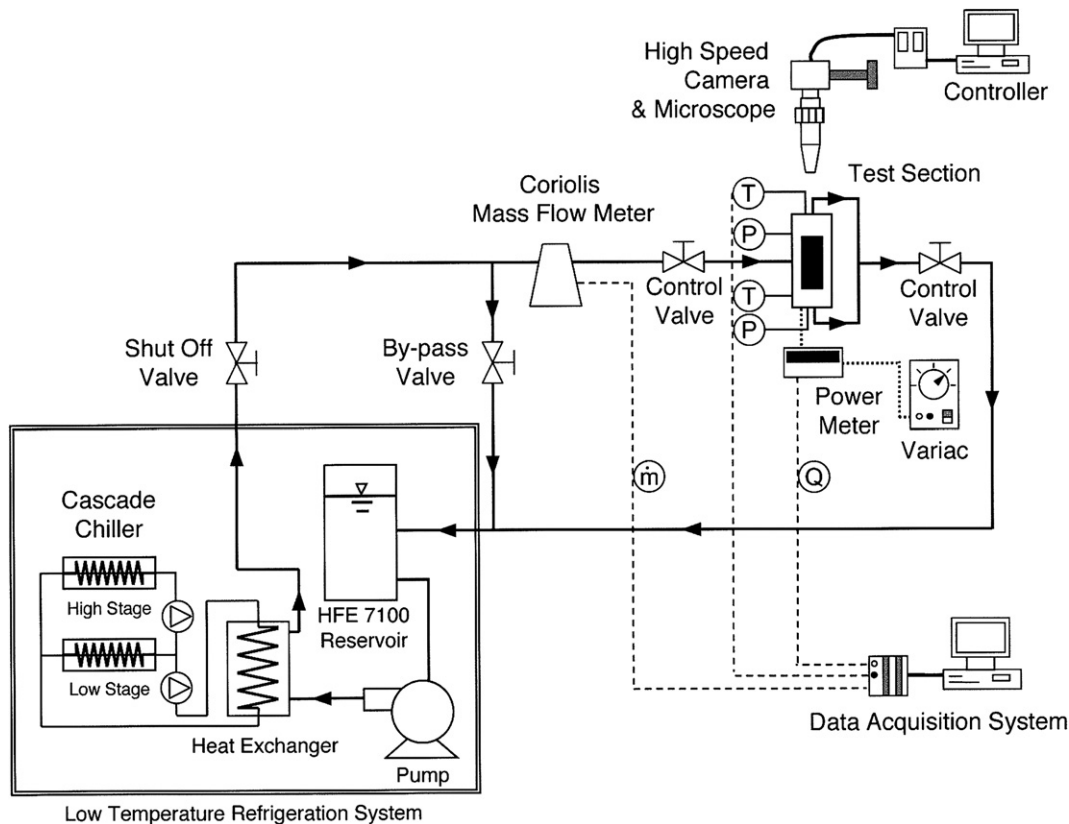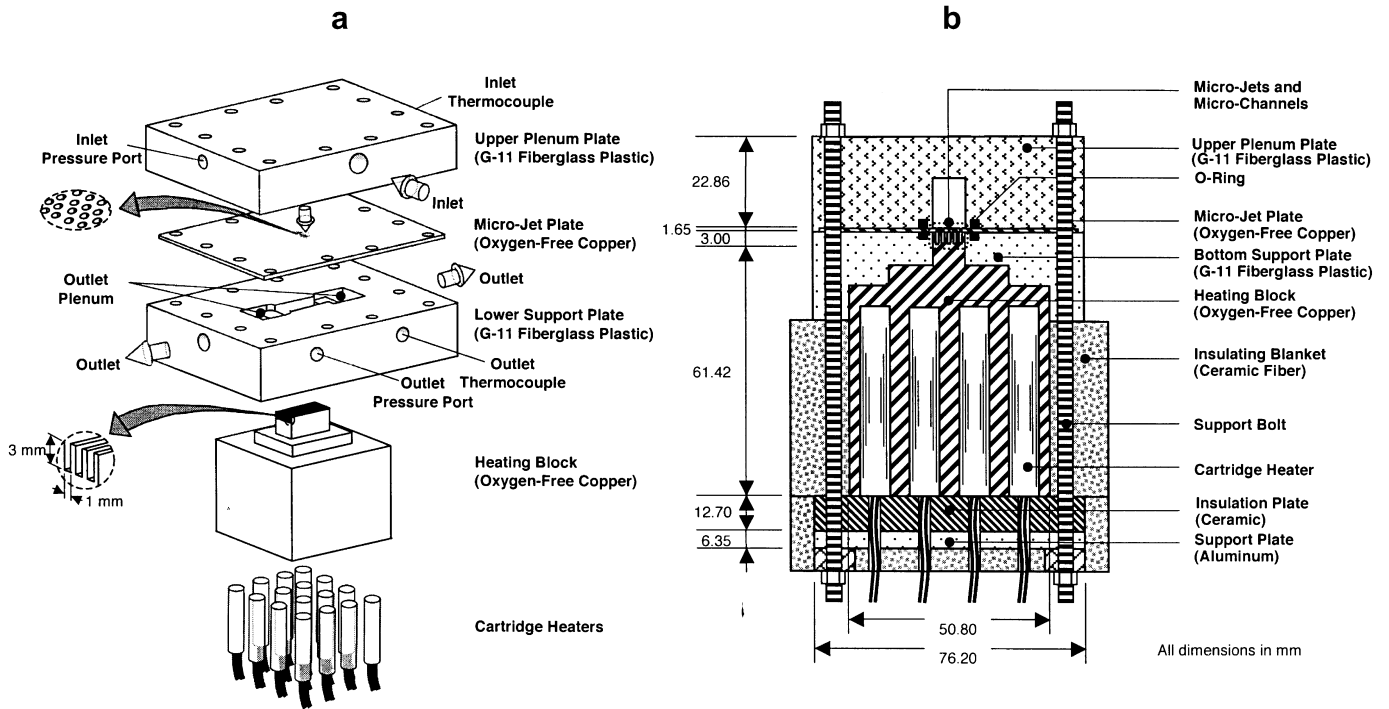

Fig. 1. Schematic of flow loop.

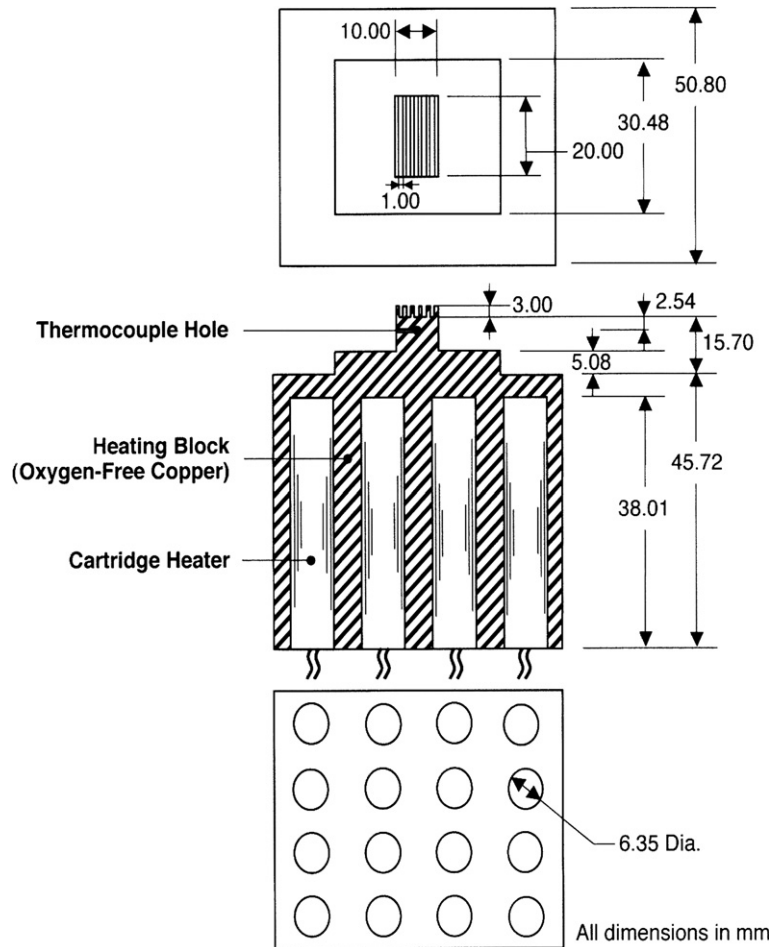Fig. 2. (a) Test module construction. (b) Cross-section of module assembly.

Fig. 3. Details of copper heating block.

cartridge heaters. These heaters were connected in a combined series/parallel circuit and powered by a singe 0-110 VAC variac. Total power dissipation from the cartridge heaters was measured by a Yokogawa WT 210 wattmeter. The top plenum plate and lower support plate of the test module were fabricated from high temperature fiberglass plastic (G-11). Blanket insulation around the circumference, and solid ceramic insulation at the bottom of the copper block helped minimize heat loss to the ambient. RTV silicone rubber was applied along the interface between the heating block and lower support plate to prevent liquid leakage.

The micro-jet plate was fabricated from oxygen-free copper. Five parallel arrays of fourteen 0.39 mm diameter circular holes were drilled equidistantly within the 1 cm width facing the five micro-channels. O-rings were used to prevent liquid leakage between the jet plate and the upper plenum plate and lower support plate. An absolute pressure transducer and a type-T thermocouple were connected to the inlet plenum in the top plenum plate. Another absolute pressure transducer and a second type-T thermocouple were connected to the outlet plenums in the lower support plate. Four stainless steel pins were used to align the cover plate with the housing to ensure accurate placement of the jets relative to the micro-channels.

2.3. Measurement uncertainty

Measurement uncertainties associated with the pressure transducers, flow meter, wattmeter, and thermocouples were 0.5%, 0.1%, 0.5%, and 0.3 °C, respectively. A numerical 3-D model of the entire test module yielded a worst-case heat loss (corresponding to the lowest coolant flow rate tested) of less than 8% of the electrical power input. The heat fluxes reported in the present paper are therefore based on the measured electrical power input.

3. Numerical scheme

Fig. 4 shows a unit cell that was used in the numerical simulation of the test module. The unit cell consists of one of the five micro-channels along with the associated array of micro-jets and surrounding solid. Key dimensions of the unit cells are given in Table 1. Fig. 4 shows both top and side sectional views of the unit cell and corresponding coordinate system and key notations. Because of symmetry, a computational domain consisting of only one quarter of the unit cell is required.

Flow profiles and heat transfer characteristics of the computational domain were predicted using Fluent 6.2.16, which is based on the finite volume method (FVM) [16]. The geometry and meshes for the computational domain were generated using Gambit 2.2.30 [17]. The standard two-equation k–ε turbulent model [18] was used for closure of the Reynolds stress tensor. Solid–liquid interfaces are governed by continuities of both temperature and heat flux,

$$T_{s,\Gamma} = T_{f,\Gamma} \tag{1}$$

and

$$-k_s \frac{\partial T_s}{\partial n}\bigg|_{\Gamma} = -k_f \frac{\partial T_f}{\partial n}\bigg|_{\Gamma}. \tag{2}$$

Conservation equations are expressed in the Cartesian tensor notation for steady, turbulent and incompressible flow with constant properties as follows.

For the fluid region:

$$\frac{\partial U_i}{\partial x_i} = 0, \tag{3}$$

$$\rho_f U_j \frac{\partial U_i}{\partial x_j} = -\frac{\partial P}{\partial x_i} + \frac{\partial}{\partial x_j}\left((\mu_f + \mu_t)\frac{\partial U_i}{\partial x_j}\right), \tag{4}$$

and

$$\rho_f c_{p,f} U_j \frac{\partial T}{\partial x_j} = \frac{\partial}{\partial x_j}\left(\left(k_f + \frac{c_{p,f}\mu_t}{Pr_t}\right)\frac{\partial T}{\partial x_j}\right), \tag{5}$$

where

$$\mu_t = \frac{C_\mu \rho_f k^2}{\varepsilon}, \tag{6}$$

$$\rho_f U_j \frac{\partial k}{\partial x_j} = \frac{\partial}{\partial x_j}\left(\left(k_f + \frac{\mu_t}{\sigma_k}\right)\frac{\partial k}{\partial x_j}\right) + G - \rho_f \varepsilon, \tag{7}$$

and

$$\rho_f U_j \frac{\partial \varepsilon}{\partial x_j} = \frac{\partial}{\partial x_j}\left(\left(k_f + \frac{\mu_t}{\sigma_\varepsilon}\right)\frac{\partial \varepsilon}{\partial x_j}\right) + C_1 G \frac{\varepsilon}{k} - C_2 \rho_f \frac{\varepsilon^2}{k}. \tag{8}$$

The production of turbulent energy is defined as $G = -\overline{u_i u_j}\partial U_i/\partial x_j$. The following values were used for the coefficients in the above equations: $C_\mu = 0.09$, $C_1 = 1.44$, $C_2 = 1.92$, $\sigma_k = 1.0$, $\sigma_\varepsilon = 1.3$, and $Pr_t = 0.85$.

For the solid region:

$$U_i = 0, \tag{9}$$

and

$$\frac{\partial}{\partial x_j}\left(k_s \frac{\partial T}{\partial x_j}\right) = 0. \tag{10}$$

Heat transfer in the unit cell is a conjugate one combining conduction and convection effects. Boundary conditions were specified as follows:

$$u = 0, \quad v = 0, \quad w = -U_{\text{jet}}, \quad \text{and}$$
$$T = T_{\text{in}}, \quad \text{for the jet inlet} \tag{11}$$

$$\dot{m} = \dot{m}_{\text{in}}, \quad \frac{\partial v}{\partial x} = 0, \quad \frac{\partial w}{\partial x} = 0, \quad \text{and}$$

$$\frac{\partial T}{\partial x} = 0, \quad \text{for the channel outlet.} \tag{12}$$

For the solid regions, a constant heat flux was applied along the copper bottom boundary of the unit cell:

$$-k_s \frac{\partial T}{\partial z} = q''_{\text{eff}}, \tag{13}$$

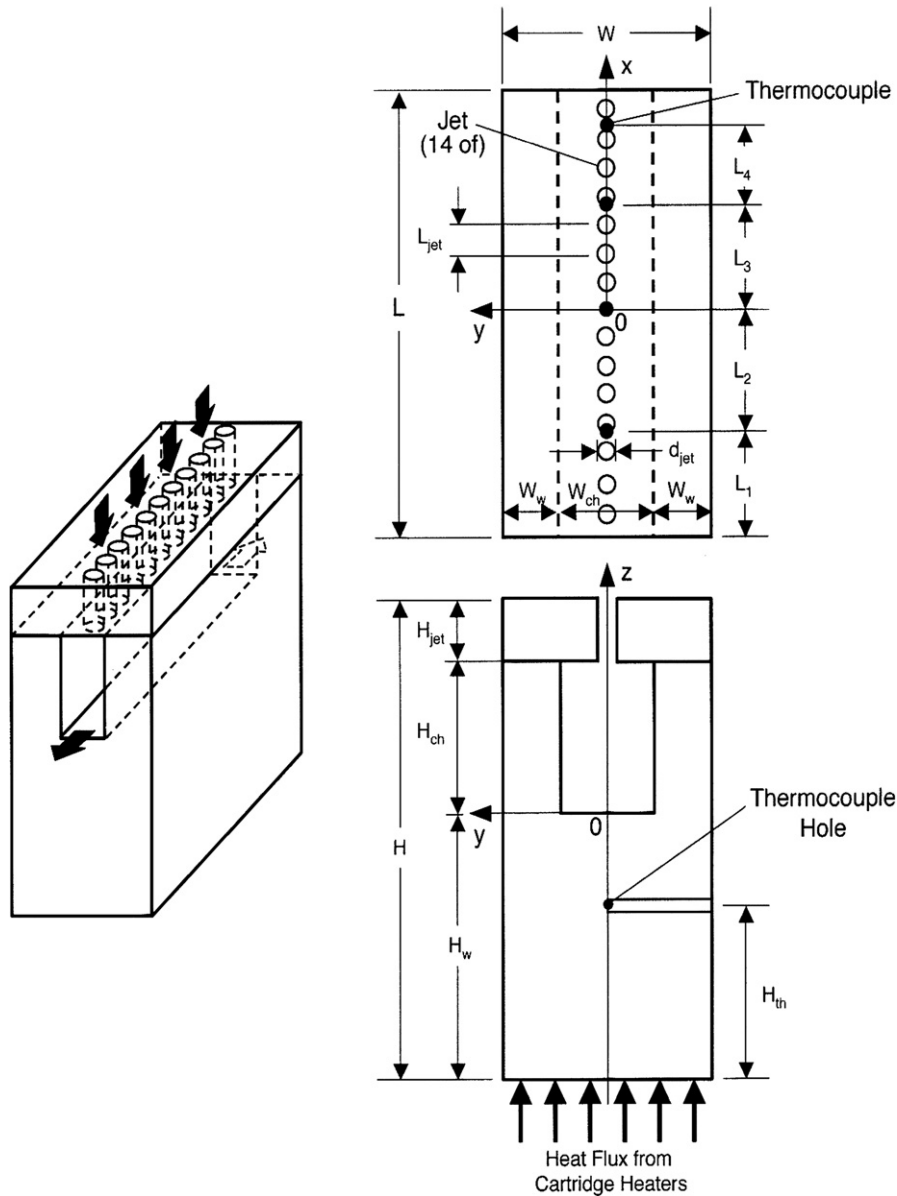where q''_{eff} was determined from measured electrical power input

Fig. 4. Schematic of unit cell consisting of single row of circular micro-jets and single micro-channel.

Table 1
Dimensions of unit cell

L (mm)	L_1 (mm)	L_2 (mm)	L_3 (mm)	L_4 (mm)	W (mm)	W_{ch} (mm)	W_w (mm)	H (mm)	H_{jet} (mm)	H_{ch} (mm)	H_w (mm)	H_{th} (mm)	D_{jet} (mm)	L_{jet} (mm)
20.00	4.00	6.00	3.00	6.00	1.83	1.00	0.42	14.27	1.65	3.00	7.62	5.08	0.39	1.43

$$q''_{\text{eff}} = \frac{P_W}{A_t}. \tag{14}$$

A zero heat flux condition was applied to all solid thermal boundaries except the interfaces between fluid and copper. The SIMPLE (Semi-Implicit Method for Pressure-Linked Equations) algorithm by Patankar [19] was used to couple velocities and pressure. A total of 593,460 mesh cells were used in the numerical simulation.

4. Numerical results

4.1. Effects of micro-channel geometry

As discussed earlier, high temperatures and large spatial temperature gradients are two key obstacles to the implementation of many seemingly effective high-flux cooling schemes [3]. In this study, the effects of micro-channel

geometry on both maximum surface temperature and spatial temperature variations were investigated for different values of micro-jet velocity in pursuit of superior cooling geometry.

Referring to Fig. 4, the performance of the hybrid configuration was examined by varying two key geometrical parameters: micro-channel width (W_{ch}) and micro-channel height (H_{ch}). The performance predictions were repeated for three jet velocities, 1, 5 and 10 m/s for an inlet HFE 7100 liquid temperature of 0 °C and a heat flux of $q''_{eff} = 300$ W/cm². Both the diameter and pitch of the circular jets were held constant in this parametric study. Geometrical parameters used in the numerical study are summarized in Table 2.

Fig. 5 shows the parametric effects of micro-channel height for a fixed width of $W_{ch} = 1$ mm and three jet velocities. Notice the large overall decrease in surface temperature as jet velocity is increased from $U_{jet} = 1$ to 10 m/s caused by the large dependence of the convective heat transfer coefficient on jet velocity. For $U_{jet} = 5$ and 10 m/s, Fig. 5 shows an advantageous decrease in the maximum surface temperature with decreasing channel height. By reducing channel height, the jet flow is better able to penetrate the liquid flow in the micro-channel, and the impingement effect is felt more strongly at the surface. However, the decrease in maximum surface temperature realized by reducing micro-channel height is accompanied by more appreciable temperature gradients both locally and along the entire length of the micro-channel. The local gradients are the result of the aforementioned strong impingement effects, while the overall gradient is due to increased flow rate along the micro-channel. However, Fig. 5a shows reducing micro-channel height from 3 to 1 mm *increases* surface temperature.

To explain these seemingly opposite trends, streamline plots were generated for the smallest micro-channel height of $H_{ch} = 1$ mm for $U_{jet} = 1$ m/s, Fig. 6a, and $U_{jet} = 5$ m/s, Fig. 6b. Notice in Fig. 6a for the low velocity case that while the upstream jet (close to central region of micro-channel, where flow rate is zero) can easily impact the surface, its spent fluid makes it difficult for the second jet to penetrate towards the surface. The spent fluid from the first and second jets makes it even more difficult for the third jet to reach the surface, and so on. On the other hand, Fig. 6b shows that despite the increasing flow rate of spent fluid from upstream, jets at $U_{jet} = 5$ m/s are better able to penetrate the micro-channel flow. In other words, heat removal is dominated more by micro-channel flow at $U_{jet} = 1$ m/s and by jet impingement at $U_{jet} = 5$ m/s. Clearly, the effects of jet impingement must diminish even at $U_{jet} = 5$ m/s had longer micro-channels been tested. For the lower jet veloc-
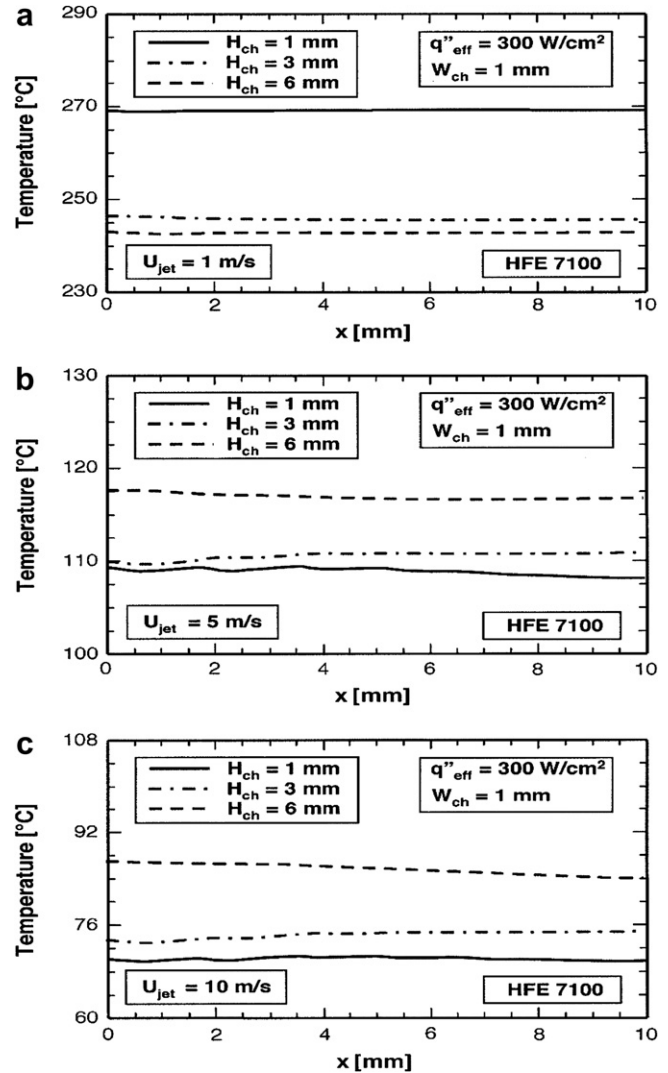

Fig. 5. Numerical predictions of the effects of micro-channel height on surface temperature for jet velocities of (a) $U_{jet} = 1$ m/s, (b) $U_{jet} = 5$ m/s, and (c) $U_{jet} = 10$ m/s.

ity, the reduced surface temperature achieved by increasing micro-channel height from 1 to 3 mm (see Fig. 5a) is apparently the result of the increased heat transfer area available for the micro-channel flow.

Fig. 7 shows the effects of micro-channel width, W_{ch}, on surface temperature for $H_{ch} = 3.0$ mm and $U_{jet} = 5$ m/s while maintaining a fixed pitch of $W = 1.83$ mm between micro-channels. As shown in Fig. 4, increasing W_{ch} decreases the micro-channel wall thickness W_w. Fig. 7 shows increasing W_w by reducing W_{ch} from 1.4 to 1.0 mm decreases both surface temperature and temperature gradient along the micro-channel. This behavior is believed to be the result of the increased contribution of conduction through the thicker sidewalls.

Using these parametric trends of micro-channel geometry as a guide to achieving favorable cooling performance, experiments were performed using the geometry detailed in Table 1 subject to the operating conditions given in Table 3.

Table 2
Dimensions tested in numerical parametric study

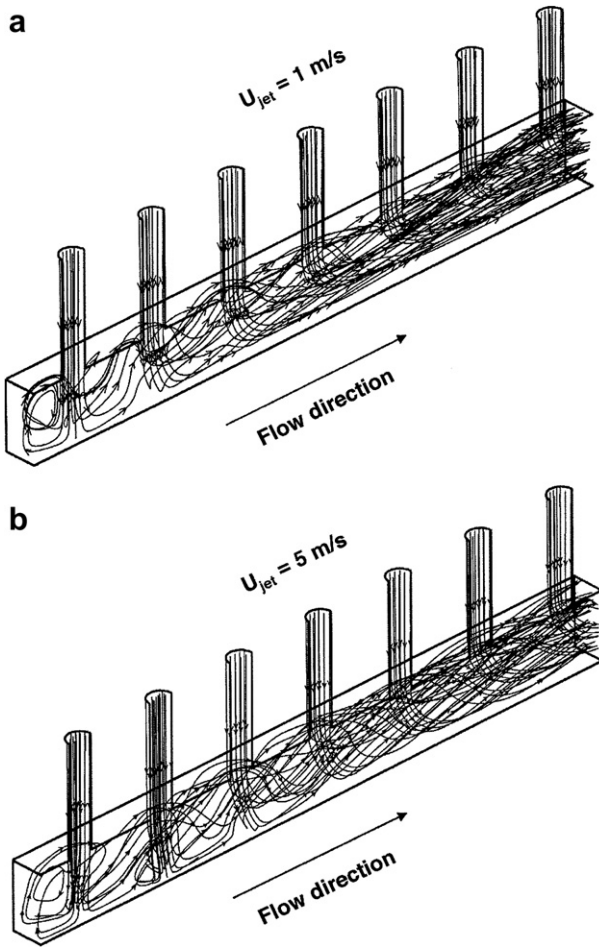| H_{ch} (mm)	W_{ch} (mm)	D_{jet} (mm)	U_{jet} (m/s)
1.00, 3.00, 6.00	1.00, 1.40	0.39	1, 5, 10

Fig. 6. Streamline plots for $H_{ch} = 1$ mm, $W_{ch} = 1$ mm and jet velocities of (a) $U_{jet} = 1$ m/s and (b) $U_{jet} = 5$ m/s.
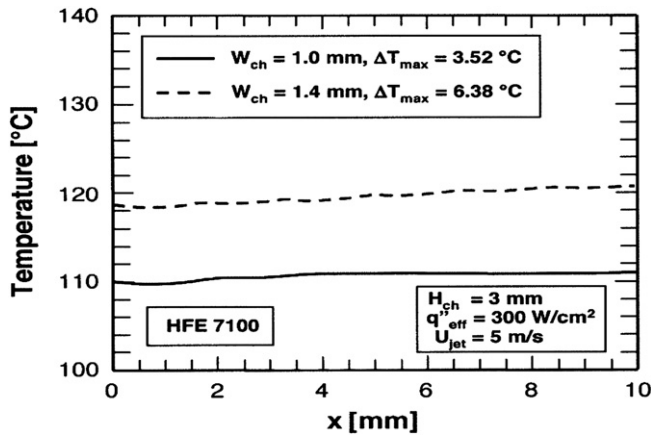

Fig. 7. Numerical predictions of the effects of micro-channel width on surface temperature for $U_{jet} = 5$ m/s and $H_{ch} = 3$ mm.

Table 3
Experimental operating conditions

Working fluid	Inlet temperature T_{in} (°C)	Inlet velocity U_{jet} (m/s)	Effective heat flux q''_{eff} (W/cm^2)
HFE 7100	−40 to 20	0.85–4.70	16.1–304.9

5. Experimental results

5.1. Overall cooling performance

As indicated earlier, three key objectives of the new hybrid cooling scheme are (1) dissipating large heat fluxes, (2) maintaining low surface temperatures, and (3) reducing surface temperature gradients. Fig. 9 shows thermocouple readings of the copper heating block as a function of jet Reynolds number for $q''_{eff} = 50$ and 91 W/cm^2. Clearly evident in this figure is the advantageous effect of increasing Re_{jet} at reducing surface temperature for a given heat flux. There is also a slight decrease in temperature gradient between thermocouples at higher Re_{jet}. However, both surface temperature and temperature gradient increase with increasing heat flux.

Overall, axial surface temperature variations over the entire single-phase cooling region up to 50 W/cm^2 were less than 1.5 °C. Remarkably, the present experiments reached a single-phase cooling heat flux of 304.9 W/cm^2. This condition was achieved with $T_{in} = -40$ °C and $U_{jet} = 4.42$ m/s. Yet even at this high heat flux, the average surface temperature was only 68.0 °C, well below the maximum recommended temperature for modern high performance electronic devices.

5.2. Comparison of numerical predictions and experimental results

Fig. 8 shows excellent agreement between numerical predictions of temperature along the thermocouple line in the copper heating block and the four thermocouples measurements. This agreement proves the standard k–ε model accurately predicts the heat transfer performance of the hybrid cooling scheme.

6. Correlation of heat transfer data

A new single-phase heat transfer correlation is sought for the new hybrid cooling scheme. Such a correlation can serve as a convenient tool for design of electronic
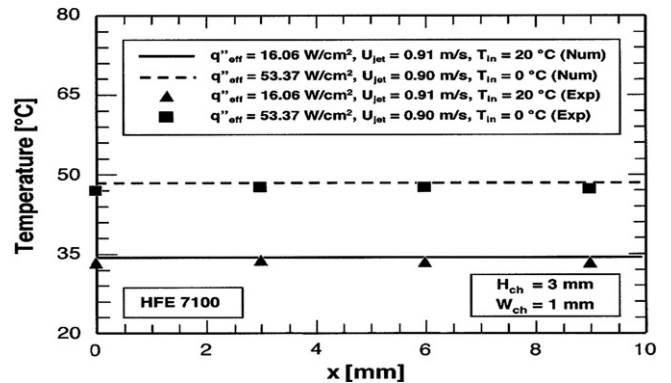

Fig. 8. Comparison of numerical predictions of temperatures along thermocouple line and measured temperatures.

modules utilizing the new hybrid cooling scheme, eliminating the need for much of the aforementioned numerical modeling.

A superpositioning technique originally developed by Wadsworth and Mudawar [6] for slot jets can be tailored to hybrid configurations where different cooling mechanisms dominate different portions of the surface. This technique was quite effective at correlating their single-phase data, and was later used successfully to correlate data for multiple slot jets [20] as well as the present authors' own data for the aforementioned hybrid slot jet/micro-channel cooling scheme [15].

This technique consists of applying different correlations of the same general form

$$\frac{\overline{Nu}}{Pr_{\mathrm{f}}^{0.4}} = f(Re) \tag{15}$$

to the different surface regions. Fig. 10 illustrates for a single jet cell the different surface regions associated with a single jet: an impingement region, two identical bottom wall regions on either side of the impingement region, and a micro-channel flow region. The micro-channel flow region encompasses upstream and downstream bottom wall regions shown in Fig. 10, as well as the sidewalls and top wall of the micro-channel for the entire jet cell
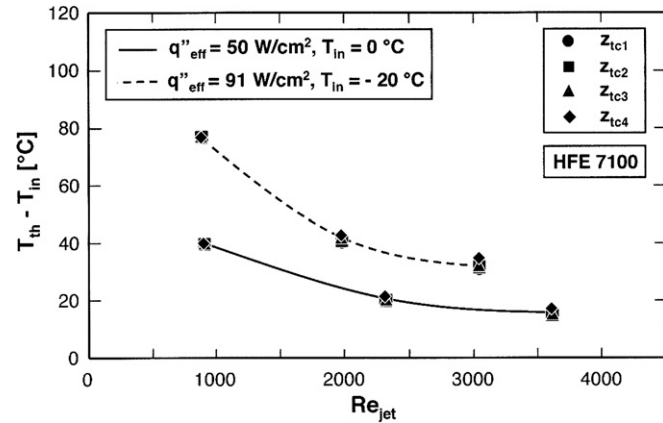

Fig. 9. Thermocouple readings in copper heating block versus jet Reynolds number for different heat fluxes and inlet temperatures.
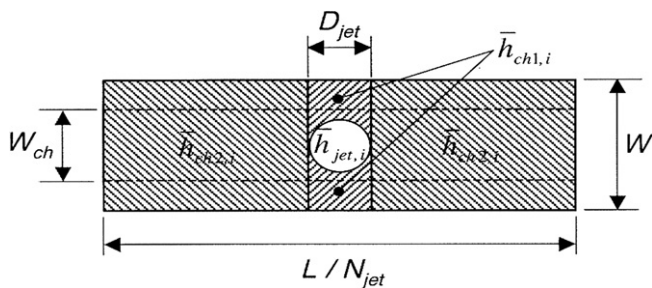

Fig. 10. Schematic of superpositioning technique for correlating single-phase heat transfer data.

(top wall is thermally conducting in present cooling module). Assuming surface temperature is uniform across the entire wetted surface, the superpositioning technique yields the following relation for overall heat transfer coefficient, $\bar{h}_L$:

$$\bar{h}_L p_h L = 2 \sum_{i=1}^{N_{\mathrm{jet}}/2} \left\{ \bar{h}_{\mathrm{jet},i} \left[\frac{\pi D_{\mathrm{jet}}^2}{4} \right] + \bar{h}_{\mathrm{ch}1,i} \left[\left(W_{\mathrm{ch}} D_{\mathrm{jet}} - \frac{\pi D_{\mathrm{jet}}^2}{4} \right) \right] \right. \\ \left. + \bar{h}_{\mathrm{ch}2,i} \left[p_h \frac{L}{N_{\mathrm{jet}}} - \left(W_{\mathrm{ch}} D_{\mathrm{jet}} + \frac{\pi D_{\mathrm{jet}}^2}{4} \right) \right] \right\}, \tag{16}$$

where N_{jet} is the number of micro-jets per single microchannel and p_h the micro-channel perimeter. Since channel velocity increases away from the central jets towards the outlet due to the increased flow rate, Eq. (16) is written to allow for variations in the values of heat transfer coefficients between successive jet cells similar to those depicted in Fig. 10.

Eq. (16) can be represented in the dimensionless form

$$\overline{Nu}_L = \frac{\bar{h}_L L}{k_{\mathrm{f}}} = 2 \sum_{i=1}^{N_{\mathrm{jet}}/2} \left\{ \left[\frac{\bar{h}_{\mathrm{jet},i} \left(\frac{\pi D_{\mathrm{jet}}^2}{4 p_h} \right)}{k_{\mathrm{f}}} \right] + \left[\frac{\bar{h}_{\mathrm{ch}1,i} \left(\frac{W_{\mathrm{ch}} D_{\mathrm{jet}} - \frac{\pi D_{\mathrm{jet}}^2}{4}}{p_h} \right)}{k_{\mathrm{f}}} \right] \right. \\ \left. + \left[\frac{\bar{h}_{\mathrm{ch}2,i} \left[\frac{L}{N_{\mathrm{jet}}} - \frac{W_{\mathrm{ch}} D_{\mathrm{jet}}}{p_h} \left(1 + \frac{\pi D_{\mathrm{jet}}^2}{4} \frac{1}{W_{\mathrm{ch}} D_{\mathrm{jet}}} \right) \right]}{k_{\mathrm{f}}} \right] \right\}. \tag{17}$$

The Reynolds used to characterize the heat transfer in the different surface regions depicted in Fig. 10 are defined as

$$Re_{\mathrm{jet},i} = \frac{U_{\mathrm{jet}} D_{\mathrm{jet}}}{v_{\mathrm{f}}}, \tag{18a}$$

$$Re_{\mathrm{ch}1,i} = \frac{U_{\mathrm{ch}1,i} \left(\frac{W_{\mathrm{ch}} D_{\mathrm{jet}} - \frac{\pi D_{\mathrm{jet}}^2}{4}}{p_h} \right)}{v_{\mathrm{f}}}, \tag{18b}$$

and

$$Re_{\mathrm{ch}2,i} = \frac{U_{\mathrm{ch}2,i} \left[\frac{L}{N_{\mathrm{jet}}} - \frac{W_{\mathrm{ch}} D_{\mathrm{jet}}}{p_h} \left(1 + \frac{\pi D_{\mathrm{jet}}^2}{4} \frac{1}{W_{\mathrm{ch}} D_{\mathrm{jet}}} \right) \right]}{v_{\mathrm{f}}}. \tag{18c}$$

The characteristic velocity in Eq. (18b) is assumed equal to the jet velocity due to the strong attachment of wall jet in that region and the Bernoulli assumption

$$U_{\mathrm{ch},i} = U_{\mathrm{jet}}. \tag{19}$$

The characteristic velocity in $Re_{\mathrm{ch}2,i}$ is determined from continuity, accounting for the gradual increase in flow rate away from the center of the micro-channel

$$U_{\mathrm{ch}2,i} = \frac{U_{\mathrm{jet}} \frac{\pi D_{\mathrm{jet}}^2}{4} i}{W_{\mathrm{ch}} H_{\mathrm{ch}}}. \tag{20}$$

Therefore the heat transfer correlation can now be written as

$$\frac{\overline{Nu}_L}{Pr_f^{0.4}} = 2\sum_{i=1}^{N_{jet}/2} \left\{ C_1 Re_{jet}^a \left(\frac{D_{jet}}{p_h}\right) + C_2 Re_{ch1}^b + C_3 Re_{ch2,i}^c \right\}$$

$$= 2\sum_{i=1}^{N_{jet}/2} \left\{ C_1 Re_{jet}^a \left(\frac{D_{jet}}{p_h}\right) + C_2 Re_{jet}^b \left(\frac{W_{ch}D_{jet} - \frac{\pi D_{jet}^2}{4}}{p_h D_{jet}}\right)^b \right.$$

$$+ C_3 Re_{jet}^c \left\{ \frac{\frac{\pi D_{jet}^2}{4}}{W_{ch}H_{ch}} \left[\frac{1}{N_{jet}} \frac{L}{D_{jet}}\right. \right.$$

$$\left. \left. \left. - \frac{W_{ch}}{p_h} \left(1 + \frac{\pi D_{jet}^2}{4} \frac{1}{W_{ch}D_{jet}}\right)\right] i \right\}^c \right\}$$

$$= C_1 Re_{jet}^a \left(\frac{D_{jet}}{p_h}\right) N_{jet} + C_2 Re_{jet}^b \left(\frac{W_{ch}D_{jet} - \frac{\pi D_{jet}^2}{4}}{p_h D_{jet}}\right)^b N_{jet}$$

$$+ 2C_3 Re_{jet}^c \left\{ \frac{\frac{\pi D_{jet}^2}{4}}{W_{ch}H_{ch}} \left[\frac{1}{N_{jet}} \frac{L}{D_{jet}}\right.\right.$$

$$\left.\left. - \frac{W_{ch}}{p_h} \left(1 + \frac{\pi D_{jet}^2}{4} \frac{1}{W_{ch}D_{jet}}\right)\right]\right\}^c$$

$$\times \left\{ 1^c + 2^c + \cdots + (N_{jet}/2)^c \right\}. \tag{21}$$

The exponent, a, corresponding to the impingement term is set to 0.5, which is the value recommended for the impingement zone of a jet [6]. The remaining empirical constants were determined from a least-squares fit to the experimental data, resulting in the following correlation for the hybrid cooling scheme:

$$\frac{\overline{Nu}_L}{Pr_f^{0.4}} = 63.41 Re_{jet}^{0.5} \left(\frac{D_{jet}}{p_h}\right) N_{jet}$$

$$+ 0.183 Re_{jet}^{0.199} \left(\frac{W_{ch}D_{jet} - \frac{\pi D_{jet}^2}{4}}{p_h D_{jet}}\right)^{0.199} N_{jet}$$

$$+ 0.197 Re_{jet}^{0.654} \left\{ \frac{\frac{\pi D_{jet}^2}{4}}{W_{ch}H_{ch}} \left[\frac{1}{N_{jet}} \frac{L}{D_{jet}}\right.\right.$$

$$\left.\left. - \frac{W_{ch}}{p_h} \left(1 + \frac{\pi D_{jet}^2}{4} \frac{1}{W_{ch}D_{jet}}\right)\right]\right\}^{0.654}$$

$$\times \left\{ 1^{0.654} + 2^{0.654} + \cdots + (N_{jet}/2)^{0.654} \right\}. \tag{22}$$

Notice that D_{jet}, H_{ch}, W_{ch}, p_h, L and N_{jet} are purposely retained in Eq. (22) rather than replaced with the values used in the present experimental study. This is intended to allow Eq. (22) to be used for a hybrid scheme with different values for these parameters.

Fig. 11 shows Eq. (22) fits the present single-phase data with a mean absolute error (MAE) of only 6.04%, with all data points falling within a ±20% error range.
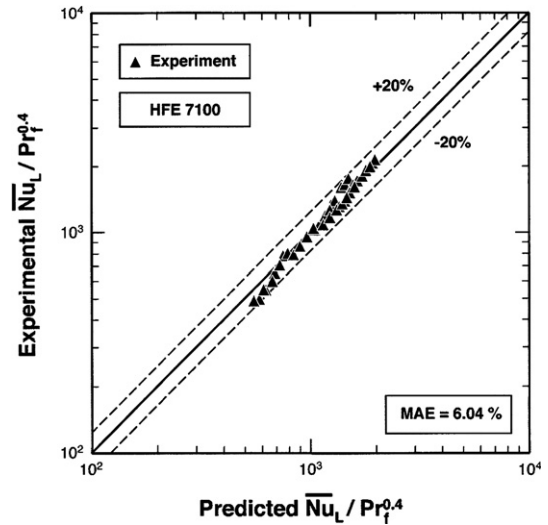

Fig. 11. Comparison of predictions of single-phase heat transfer correlation and experimental data.

7. Conclusions

A new hybrid cooling scheme was developed that combines the benefits of both micro-jet impingement and micro-channel flow. The performance of the cooling scheme was further enhanced by indirect refrigeration cooling. Numerical analysis was used to explore the effects of key parameters of the hybrid geometry. Preferred values of these parameters were used to design a test module that served to validate the predicted performance using HFE 7100 as working fluid. Key findings from the study are as follows:

1. The proposed cooling scheme involves complex interactions of circular impinging jets with micro-channel flow. Numerical results show increasing jet velocity allows jets to penetrate the micro-channel flow toward the surface, especially in shallow micro-channels, greatly decreasing the average wall temperature.
2. Excellent agreement between numerical predictions and temperature measurements proves the standard k–ε model is very effective at predicting the heat transfer performance of the hybrid cooling scheme.
3. Despite the relatively poor thermophysical properties of HFE 7100, the proposed cooling scheme is capable of achieving an unprecedented cooling performance of 304.9 W/cm^2 without phase change. This performance is realized with an inlet temperature of $T_{in} = -40$ °C and $U_{jet} = 4.42$ m/s. Further improvements in single-phase cooling performance are possible by increasing jet velocity and/or decreasing inlet temperature. Interestingly, surface temperature variations for all conditions up to 50 W/cm^2 are less than 1.5 °C.
4. A superpositioning technique is introduced that partitions the heat transfer surface into zones that are each dominated by a different heat transfer mechanism, and assigning a different heat transfer coefficient value to

each zone. Using this technique, a new correlation is developed that predicts the present HFE 7100 data with a mean absolute error of 6.04%.

Acknowledgement

References

[1] A. Naeemi, J.D. Meindl, An upper limit for aggregate I/O interconnect bandwidth of GSI chips constrained by power dissipation, in: Proceedings of IEEE International Interconnect Technology Conference, San Francisco, CA, 2004, pp. 157–159.

[2] R.R. Schmidt, B.D. Notohardjono, High-end server low-temperature cooling, IBM J. Res. Dev. 49 (2002) 739–751.

[3] I. Mudawar, Assessment of high-heat-flux thermal management schemes, IEEE Trans. Compon. Packaging Technol. 24 (2001) 122–141.

[4] H. Martin, Heat and mass transfer between impinging gas jets and solid surfaces, Adv. Heat Transfer 13 (1977) 1–60.

[5] L.M. Jiji, Z. Dagan, Experimental investigation of single-phase multi-jet impingement cooling of array of microelectronic heat sources, in: Proceedings of International Symposium on Cooling Technology for Electronic Equipment, Honolulu, HI, 1987, pp. 265–283.

[6] D.C. Wadsworth, I. Mudawar, Cooling of a multichip electronic module by means of confined two-dimensional jets of dielectric liquid, ASME J. Heat Transfer 112 (1990) 891–898.

[7] K.A. Estes, I. Mudawar, Comparison of two-phase electronic cooling using free jets and sprays, ASME J. Electron. Packaging 117 (1995) 323–332.

[8] T.J. Craft, L.J.W. Graham, B.E. Launder, Impinging jet studies for turbulence model assessment – II. An examination of the performance of four turbulence models, Int. J. Heat Mass Transfer 36 (1993) 2685–2697.

[9] T.H. Park, H.G. Choi, J.Y. Yoo, S.J. Kim, Streamline upwind numerical simulation of two-dimensional confined impinging slot jets, Int. J. Heat Mass Transfer 46 (2003) 251–262.

[10] E. Baydar, Y. Ozmen, An experimental and numerical investigation on a confined impinging air jet at high Reynolds numbers, Appl. Therm. Eng. 25 (2005).

[11] D.B. Tuckerman, R.F.W. Pease, High-performance heat sinking for VLSI, IEEE Electron. Dev. Lett. EDL-2 (1981) 126–129.

[12] S.J. Kim, D. Kim, forced convection in microstructures for electronic equipment cooling, ASME J. Heat Transfer 121 (1999) 639–645.

[13] A.G. Fedorov, R. Viskanta, Three-dimensional conjugate heat transfer in the microchannel heat sink for electronic packaging, Int. J. Heat Mass Transfer 43 (2000) 399–415.

[14] W. Qu, I. Mudawar, Experimental and numerical study of pressure drop and heat transfer in a single-phase micro-channel heat sink, Int. J. Heat Mass Transfer 45 (2002) 2549–2565.

[15] M.K. Sung, I. Mudawar, Experimental and numerical investigation of single-phase heat transfer using a hybrid jet impingement/micro-channel cooling scheme, Int. J. Heat Mass Transfer 49 (2006) 682–694.

[16] Fluent 6.2.16, User's Guide, Fluent Inc., Lebanon, NH, 2005.

[17] Gambit 2.2.30, User's Guide, Fluent Inc., Lebanon, NH, 2006.

[18] B.E. Launder, D.B. Spalding, The numerical computation of turbulent flows, Comput. Meth. Appl. Mech. Eng. 3 (1974) 269–289.

[19] S.V. Patankar, Numerical Heat Transfer and Fluid Flow, Hemisphere, Washington, DC, 1980.

[20] M.T. Meyer, I. Mudawar, C.E. Boyack, C.A. Hale, Single-phase and two-phase cooling with an array of rectangular jets, Int. J. Heat Mass Transfer 49 (2006) 17–29.